




Direct measurements of the $^{12}\text{C}+^{12}\text{C}$ reactions cross-sections towards astrophysical energies

L. Morales-Gallegos^{1,2,3,a} , M. Aliotta^{1,2}, L. Gialanella^{1,3}, A. Best^{3,5}, C. G. Bruno², R. Buompane^{1,3}, T. Davinson², M. De Cesare^{3,4}, A. Di Leva^{3,5}, A. D'Onofrio^{1,3}, J. G. Duarte^{1,3,7}, L. R. Gasques^{1,3,6}, G. Imbriani^{3,5}, G. Porzio¹, D. Rapagnani^{1,3}, M. Romoli³, F. Terrasi^{1,3}

¹ Dipartimento di Matematica e Fisica, Università degli Studi della Campania "Luigi Vanvitelli", Caserta, Italy

² SUPA, School of Physics and Astronomy, University of Edinburgh, Edinburgh, UK

³ INFN, Sezione di Napoli, Naples, Italy

⁴ Centro Italiano di Ricerche Aerospaziali, Capua, Italy

⁵ Dipartimento di Fisica "E. Pancini", Università degli Studi di Napoli "Federico II", Naples, Italy

⁶ Departamento de Física Nuclear, Instituto de Física da Universidade de São Paulo, São Paulo, Brazil

⁷ Present address: Nuclear and Particle Physics Group, Lawrence Livermore National Laboratory, Livermore, CA 94550, USA

Received: 5 June 2023 / Accepted: 26 December 2023 / Published online: 22 January 2024

© The Author(s) 2024

Communicated by Aurora Tumino

Abstract Carbon fusion reactions $^{12}\text{C}(^{12}\text{C},\text{p})^{23}\text{Na}$ and $^{12}\text{C}(^{12}\text{C},\alpha)^{20}\text{Ne}$ play a key role in the evolution of massive stars and in explosive scenarios such as type-Ia supernovae and super-bursts in binary stars. A direct determination of their cross sections is extremely challenging and discrepancies exist between different data sets in the literature. Here we report the results of a direct measurement performed at the CIRCE Tandem Accelerator Laboratory in Caserta (Italy), using $\Delta E - E$ detectors for unambiguous charge identification. Cross sections were measured in the energy range $E_{\text{c.m.}} = 2.51 - 4.36$ MeV with energy steps between 10 and 25 keV in the centre of mass. To our knowledge these represent the finest energy steps to date. Results are presented in the form of partial and summed astrophysical S -factors for individual proton- and α -particle channels. Branching ratios of individual proton- and α -particle groups were found to vary significantly with energy. Angular distributions, albeit limited to three angles, were also found to be non-isotropic, which could be a potential explanation for the discrepancies observed among different data sets. Further efforts are ongoing to extend measurements to lower energies.

1 Introduction

Carbon fusion reactions are among the most important in nuclear astrophysics because of their far-reaching impact on stellar evolution and nucleosynthesis. Recent stellar model

calculations [1–3] indicate that the existence of low-energy resonances in the carbon fusion reactions, such as the one predicted in Cooper et al. [4], would have a profound impact on the structure of massive stars. For example, an enhanced carbon-burning rate by a factor of 10 would affect the convection zone structure of a $\simeq 25 M_{\odot}$ star and thus the nucleosynthesis processes occurring in its interior [5]. This in turn would alter the final properties of the star just before its supernova explosion [2, 6], leading to smaller supernovae remnants and new values for the limiting initial stellar mass between a neutron star and a black hole [1].

An accurate knowledge of the $^{12}\text{C}+^{12}\text{C}$ fusion reaction cross sections is also essential to model X-ray bursts in binary systems [4, 7], to understand explosions on the surface of neutron stars [8], and to predict the fate of white-dwarf mergers [9, 10]. As carbon burning controls the ratio between thermonuclear- and core-collapse supernovae, the luminosity function of certain stars, and the ratio between different types of white dwarfs [1, 2, 6], it also affects the chemical enrichment of the interstellar medium arising from different types of supernova explosions.

Carbon burning takes place at typical densities of $2-5 \times 10^6$ g/cm³ [11, 12] and temperatures of 5×10^8 K, corresponding to an energy range of interest, the Gamow window, $E_{\text{c.m.}} = 1.5 \pm 0.3$ MeV [13]. At these energies, the $^{12}\text{C}+^{12}\text{C}$ reactions proceed through the $^{23}\text{Na}+\text{p}$ ($Q = 2.24$ MeV) and $^{20}\text{Ne}+\alpha$ channels ($Q = 4.62$ MeV), while the $^{23}\text{Mg}+\text{n}$ ($Q =$

^ae-mail: moralesgallegos@na.infn.it (corresponding author)

-2.62 MeV) channel is closed.¹ At higher energies the neutron channel opens but its rate is about two orders of magnitude lower than that of the proton and alpha channels [15], thus reducing the relevant study of the $^{12}\text{C}+^{12}\text{C}$ reaction to the α and p channels alone. Since the Gamow window for the $^{12}\text{C}+^{12}\text{C}$ reactions is much lower than the height of the Coulomb barrier (6.3 MeV), carbon-fusion cross sections are very small ($\ll 10^{-9}$ b) and extremely difficult to measure in the laboratory [16, 17]. The extrapolation of high energy data to the relevant astrophysical energy is further made uncertain by the presence of low energy resonances of still debated origin [18–22]. In addition, direct measurements are hindered by the intense beam induced background on ^1H impurities in the target [23].

Considerable efforts have been made over the past four decades to determine the $^{12}\text{C}+^{12}\text{C}$ reactions cross-sections with the precision required for astrophysics. Experiments were performed using either charged particle spectroscopy [14, 24–26], gamma-ray spectroscopy [16, 27–34] or a combination of both [35–37]. Data at $E_{\text{c.m.}} < 3.0$ MeV still carry large uncertainties and show significant discrepancies between different data sets. Furthermore, no direct measurement has been possible at energies below $E_{\text{c.m.}} = 2.14$ MeV. As a result, the extrapolation of the astrophysical S factor into the Gamow window remains highly uncertain [18–22].

Recently, low energy cross sections for the $^{12}\text{C}+^{12}\text{C}$ reactions [38] obtained using an indirect approach based on the Trojan Horse Method, sparked an intense debate [39, 40], and further direct experimental investigations are therefore required.

Here we report the results of a direct thick-target measurement in the energy range $E_{\text{c.m.}} = 2.51\text{--}4.36$ MeV and under controlled target-temperature conditions to minimise deuterium contaminants as a first step towards measurements in the region of astrophysical energies.

The paper is organised as follows: after a brief description of the experimental setup and procedures (Sects. 2, 3), we discuss the data analysis to arrive at partial and total cross sections and \tilde{S} factors for individual proton- and alpha-channels (Sects. 3 and 4). Discussions and conclusions are presented in Sects. 5 and 6.

2 Experimental setup

The experiment was performed at the 3 MV Pelletron Tandem Accelerator Laboratory of the Centre for Isotopic Research on Cultural and Environmental heritage (CIRCE) at the Department of Mathematics and Physics of the University of Campania “Luigi Vanvitelli” in Caserta, Italy.

¹ Channel $^{24}\text{Mg}+\gamma$ is open, but it is orders of magnitude less intense than the proton- and α -channels [14].

The accelerator is coupled to a caesium sputter ion-source loaded with 2 mm inner diameter Al cathodes filled with commercial graphite pellets and capable of delivering ^{12}C -beam currents of up to 20 pA on target. The accelerator beam-transport system comprises a series of magnetic and electrostatic filters to deliver beams of sufficient mass ($\Delta M/M = 1.38 \times 10^{-3}$) and energy ($\Delta E/E = 1.43 \times 10^{-3}$) resolution [41]; For example, in $^{14}\text{C}/^{12}\text{C}$ isotopic ratio measurements, machine background was found to be smaller than 5×10^{-16} .

Full details on the experimental setup used for the $^{12}\text{C}+^{12}\text{C}$ experiment are reported in [42] and briefly described below. A large scattering chamber was used to house the carbon targets and the detection system and was enclosed in a sealed Plexiglas structure continuously flushed with dry nitrogen at a pressure slightly higher than atmospheric. The enclosure served to minimise contamination of low-mass species (mostly hydrogen and deuterium) inside the scattering chamber through inevitable air leaks. Leaks of the ICs into the chamber were monitored by means of a Pfeiffer quadrupole mass spectrometer (QMS). Non-negligible leaks would be reflected in a pressure change in the detectors and scattering chamber. We did not observe any leak in the 10^{-7} mbar region. For the ICs, CF_4 gas was preferred to other gases (e.g. isobutane) since it does not contain hydrogen.

A highly ordered pyrolytic graphite (HOPG) target (1 mm thick, 10 mm diameter, 99.99% purity) was mounted on a water-cooled target ladder and surrounded by a plastic 3D-printed hollow sphere with several opening ports (25×25 mm² each) to allow for the passage of the beam and of the particles to be detected (as shown in Fig. 1). The sphere was coated with conductive paint and kept at -300 V for electron suppression, thus allowing for a correct beam-current reading directly on target. Typical beam currents on target were of few tens of μA resulting in target temperatures of up to ~ 1200 °C, depending on beam intensity and cooling water flow [42]. The target temperature was constantly monitored by means of a thermo-camera mounted outside the scattering chamber and facing the target through a germanium window sensitive to the operational wavelengths of the thermo-camera (7.5–13 μm).

The pressure in the scattering chamber was maintained below 5×10^{-7} mbar by means of an oil-free turbo- and scroll-pump system, in combination with a cold finger kept at LN_2 temperature and protruding from the beam line to 5 cm from the target.

The detection system consisted of a two-stage detector array GASTLY (GAs Silicon Two-Layer sYstem) specifically designed to fulfil the requirements of charged particle identification from the $^{12}\text{C}+^{12}\text{C}$ reactions. The array can accommodate up to eight $\Delta E - E$ modules, each comprising an ionisation chamber (IC, ΔE stage) and a large area silicon strip detector (SSD, E_{rest} stage). Further details on

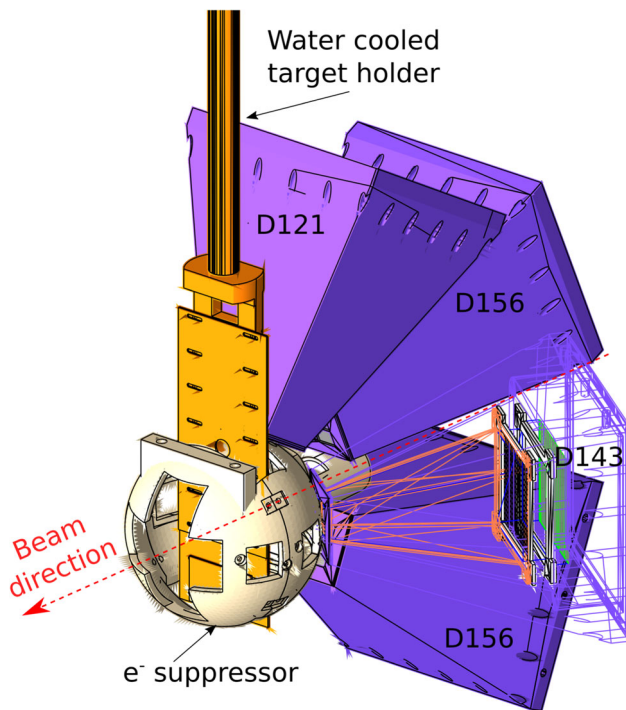


Fig. 1 Sketch of the GASTLY detectors arrangement. The four GASTLY detectors are shown along with the target holder and the sphere surrounding it for electron suppression purposes. Detector D143 is shown in wireframe to reveal its internal components (for further details see [43])

the full detector array and its commissioning are reported in [43]. Briefly, each module consists of an aluminium truncated pyramidal structure with square base, hosting the IC and the SSD detectors. The IC is equipped with an entrance Havar window ($23 \times 23 \text{ mm}^2$ large and $2.6 \pm 0.2 \text{ }\mu\text{m}$ thick) acting as a cathode; an aluminised Mylar foil ($52.5 \times 52.5 \text{ mm}^2$, $1.6 \pm 0.2 \text{ }\mu\text{m}$ thick, metallised with $50 \mu\text{m}/\text{cm}^2$ Al) acting as an anode and placed 116 mm behind the Havar window; and a Frisch grid, consisting of a mesh of gold-coated tungsten wires ($20 \text{ }\mu\text{m}$ diameter). The IC was operated with CF_4 maintained at a constant pressure (within $\pm 0.05 \text{ mbar}$) by means of an automatic system [43]. The second stage of each GASTLY module consists of a large ($58.0 \times 58.0 \text{ mm}^2$ active area, $300 \pm 15 \text{ }\mu\text{m}$ thick) silicon strip detector [44]. For the present study, however, the silicon detector was used as a single pad. In order to minimise electronic and environmental electromagnetic noise that would affect the detection of low energy particles, the GASTLY readout electronics were mounted on printed circuit boards arranged in a stack behind the silicon detector and inside the aluminium housing. The trigger of the DAQ system was generated with a logic module as the OR of the signals from the ICs and SSDs [45].

At the time of the $^{12}\text{C}+^{12}\text{C}$ measurement, only four $\Delta E - E$ modules were available: three were mounted on a vertical plane at 121° and 156° (above and below the beam axis), and

one was mounted on the horizontal plane at an angle of 143° to the beam axis (see Fig. 1). Detectors at 121° and 143° were mounted closest to the target and covered an angular range of 19° , subtending a solid angle of 80 msr. Detectors at 156° had to be placed farther away from the target to accommodate for the cold finger. They covered an angular range of 13° each, with a solid angle of 40 msr [45]. In the following, detectors are referred to as D121, D143 and D156 (after checking for their consistency, data from both detectors at this angle were merged into one data group).

3 Data taking and data analysis

Data were taken at beam energy intervals of 20–50 keV (in the laboratory system). The target temperature was maintained above 400°C (using intense beams) to reduce deuterium contamination² on target by up to 90% its original value, as found in our previous study [42]. HOPG targets used in this work are the same as those used in [26]. Such targets were monitored in that work with a HPGe detector in close geometry and no evidence of background reactions was found.

For optimal detection of α particles and protons, the ICs and SSDs detectors were calibrated using, respectively, a certified mixed ^{239}Pu - ^{241}Am α source and proton beams at various energies in the range $E_{\text{lab}} = 1\text{--}5 \text{ MeV}$ (see [45]). At high energies, the ICs were operated with CF_4 at a pressure of 35 mbar, sufficient to separate α particles and protons. At low energies, higher pressures (50 and 70 mbar) were also used to better separate protons from electronic noise in the acquired spectra.

Figure 2 shows a typical calibrated $\Delta E - E_{\text{rest}}$ matrix for detector D121 at a pressure of 35 mbar, obtained with a $^{12}\text{C}^{+3}$ beam at $E_{\text{lab}} = 8.72 \text{ MeV}$ on the HOPG target. The two loci correspond to protons and α particles from the $^{12}\text{C}(^{12}\text{C},\text{p})^{23}\text{Na}$ and $^{12}\text{C}(^{12}\text{C},\alpha)^{20}\text{Ne}$ reactions. The ROI (green polygon) represents the proton locus whilst all events with $\Delta E > 1 \text{ MeV}$ were treated as α particles. Events at the far left of the proton locus were neglected from the analysis since they are mainly spurious coincidences between α -particles completely stopped in the ionization chamber and low energy protons (very high excited states in ^{23}Na not analysed here) arriving to the silicon detector. These α -particles were identified as α_2 and not analysed in the present work.

For the analysis of each particle channel, the events of interest were selected excluding events due to electronic noise (mostly located in the bottom left corner of the $\Delta E - E_{\text{rest}}$ matrix). Depending on energy, some protons and α -particles were stopped in the IC and were therefore recorded

² In the present experimental configuration, i.e. backward detection angles, hydrogen contamination does not affect the measurement of the $^{12}\text{C}+^{12}\text{C}$ reactions (see [42] for further details).

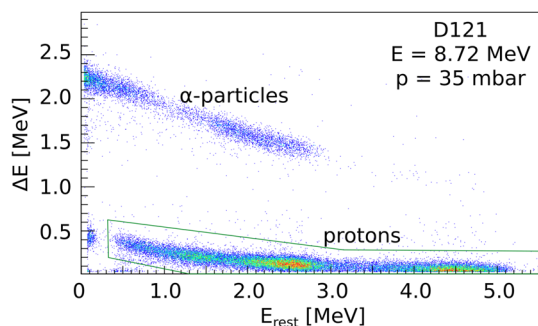


Fig. 2 Typical calibrated $\Delta E - E_{rest}$ matrix showing the α particles and protons loci. This matrix was obtained using D121 with 35 mbar of CF_4 in the IC and with a $E_{lab} = 8.72$ MeV $^{12}C^{+3}$ beam impinging on the HOPG target

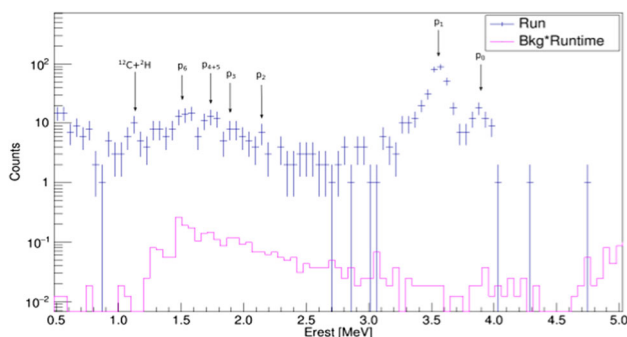


Fig. 3 Raw spectra for the proton channel taken with D156 at $E_{lab} = 7.71$ MeV (in blue) and its corresponding time-normalised background run (in pink)

with zero E_{rest} . Conversely, some protons were so energetic that their signal falls below the IC's threshold and deposited all their energy in the SSD. These events do not appear in the matrix but were all included in the analysis.

Background runs of several days³ were taken in the same experimental conditions as the $^{12}C+^{12}C$ measurements and subtracted (after time normalisation) from the corresponding proton and α -particle spectra at each beam energy. Figures 3 and 4 show typical raw spectra for the proton and α channel, respectively and the background spectra used for analysis.

In addition to the $^{1,2}H$ contamination already addressed in [42], beam-induced background on ^{13}C contaminant was also investigated, and its contribution found to be negligible ($\ll 1\%$) at all energies studied here [45].

³ 10 days at 35 mbar (used for the highest energies), 15 days at 50 mbar (used for medium-low energies) and 19 days at 70 mbar (used for the lowest energies). The statistical error of each background run $\sqrt{N_{bkg}}$ was calculated using the number of events in the regions of interest of each particle group.

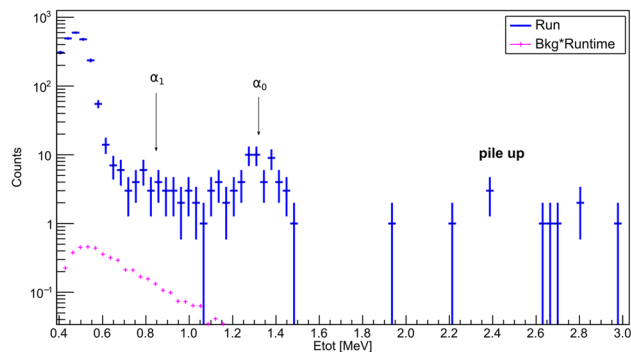


Fig. 4 Raw spectra for the α channel taken with D121 at $E_{lab} = 5.86$ MeV (in blue) and its corresponding time-normalised background run (in pink)

3.1 Fitting procedure

After background subtraction, proton and α -particle peaks from the $^{12}C+^{12}C$ reactions were identified through kinematic reconstruction (i.e., including all relevant energy losses) and via comparison with simulations [46]. In the following, we describe separately the procedure used to analyse data for each channel.

Proton channel

Given that all analysed protons at the energies used in this work arrive to the SSD, only its spectra were used in the proton analysis. Sample E_{rest} proton spectra, taken at four beam energies with D156 and at a CF_4 pressure of 35–70 mbar in the IC, are shown in Fig. 5.

Distinct proton groups are labelled according to the excitation state of the recoiling nucleus.⁴ Despite choosing experimental conditions that minimised the level of deuterium contaminants in the targets (see [42]), some deuterium-induced peaks are still visible in the proton spectra, specifically the peak around 1 MeV corresponding to the $^2H(^{12}C,p)^{13}C$ reaction. Note that, because of inverse kinematics, its position remained essentially unchanged with decreasing beam energy, while the $^{12}C+^{12}C$ proton peaks moved to lower energies as expected. Kinematics calculations show that contributions from excited states of ^{13}C would lead to protons with $E < 100$ keV. These low-energy protons would not pass through the entrance window of the ICs and as such, remain below our detection threshold. In most cases, it was possible to disentangle this beam-induced contribution from the peaks of interest, but where this was not the case, the affected proton peaks were discarded from further analysis.

⁴ Particle peaks labelled as p_0, p_1, p_2, \dots ($\alpha_0, \alpha_1, \alpha_2, \dots$) correspond to reactions in which the recoiling nuclei ^{23}Na (^{20}Ne) are left in their ground-, first-, second-excited state and so on.

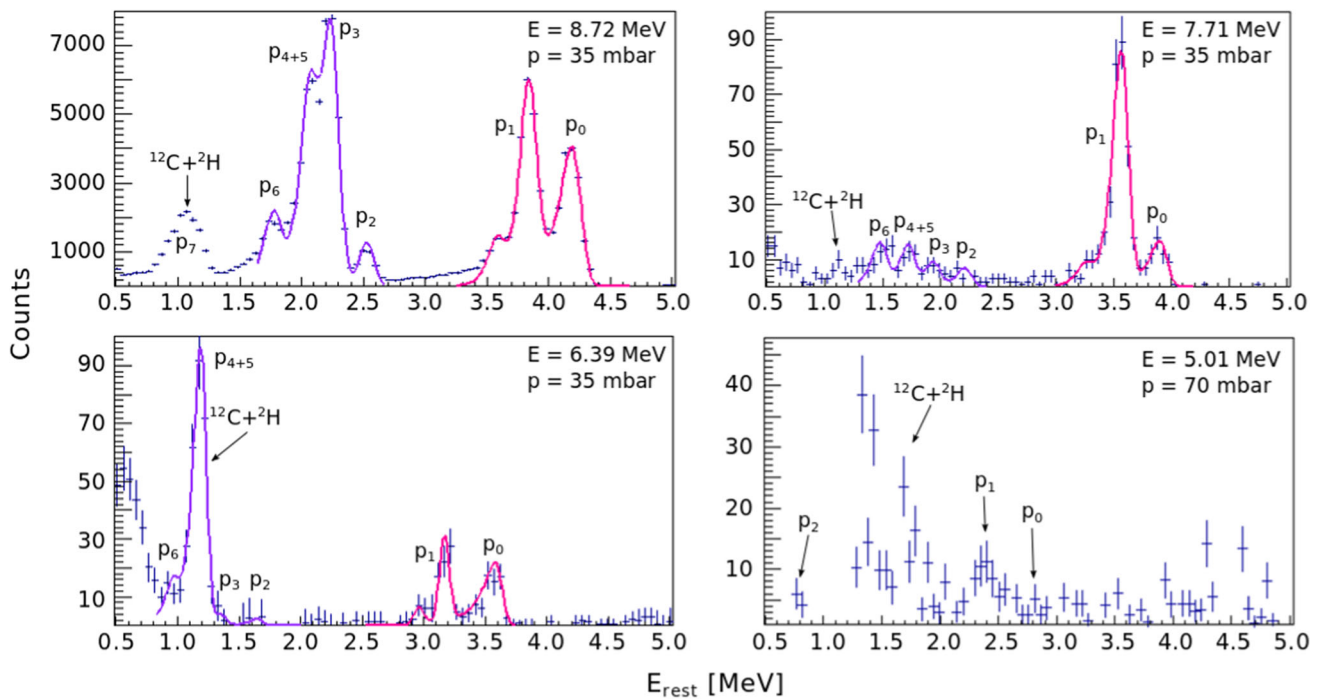


Fig. 5 Fitted sample spectra taken with D156 at four different beam energies and with 35–70 mbar of gas in the IC. Note how the various proton peaks from the $^{12}\text{C}(^{12}\text{C},\text{p})^{23}\text{Na}$ reaction shift towards lower

energies at lower beam energy (as expected) thus progressively merging with the proton peak from the $\text{d}(^{12}\text{C},\text{p})^{13}\text{C}$ direct reaction

Another peak, probably due to an electronic effect, was also observed on the lower-energy shoulder of p_1 , however its contribution cancels out when we calculate the differential yield for the cross section (as explained in Sect. 3.2).

As many proton peaks overlap (Fig. 5), the number of events within each was extracted using the maximum likelihood method from a combined fit of skewed Gaussian functions $f(x)$, each of the form:

$$f(x) = A \left(\frac{\exp\left[\frac{\sigma'^2 + 2\tau(x-\mu)}{2\tau^2}\right] \text{Erfc}\left[\frac{x-\mu+\frac{\sigma'^2}{\tau}}{\sigma'\sqrt{2}}\right]}{2\tau} \right), \quad (1)$$

where A is the amplitude of the distribution, μ and σ' are its centroid and standard deviation, τ corresponds to the shape parameter and $\text{Erfc}(x)$ is the complementary error function. Specifically, the sum of three skewed Gaussians was used to fit p_0 , p_1 and the satellite peak (where visible) at the left of p_1 , while the sum of four skewed Gaussians was used to fit p_2 , p_3 , p_{4+5} (since p_4 and p_5 cannot be separated) and p_6 . Note that the positions of the different peaks in the fit were constrained to the energy range expected on the basis of kinematic calculations taking into account energy losses in the ΔE stage and the detector passive layers using SRIM [48].

The amplitude A of each fitted individual distribution (Eq. 1) represents the net number of events N (background subtracted) associated to a given transition, allowing for the extraction of its corresponding yield [47]. The statistical uncertainty, δN , was calculated as a sum in quadrature of the statistical error in background counts, $\sqrt{N_{\text{bkg}}}$, under the relevant proton peak and the error, δA , on the parameter A .

For runs taken at beam energies $E_{\text{lab}} < 5.5$ MeV, low statistics prevented a direct identification of the proton peaks. Thus, we relied on regions of interest (ROI) identified by kinematic reconstruction at each beam energy, taking into account all energy losses. We then integrated the counts in each ROI to arrive at the net number of events N_{ROI} . Uncertainties δN were calculated by replacing δA with the statistical error $\sqrt{N_{\text{ROI}}}$.

In the present paper, results show only statistical errors. However, for a complete estimation of the uncertainties, the following sources of systematic errors should be considered: accumulated charge ($< 1\%$; corresponding to the precision of the charge integrator used [49]), solid angles (0.9–1.2%; measured as detailed in [45]) and stopping power (about 8%; given by the use of the SRIM software [48]). The covariance matrices indicated that the correlation of the estimates of the parameters is negligible.

In order to verify the validity of our peak identification procedure, two different fits were performed in various spec-

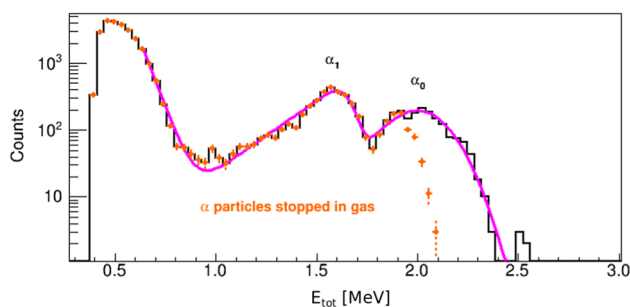


Fig. 6 Typical α ($E_{\text{tot}} = \Delta E + E_{\text{rest}}$) fitted spectrum using a sum of two skewed Gaussian functions and one exponential function. The area defined by the dashed data points ($E < 2.1$ MeV) represents the α particles stopped in the IC. This spectrum was taken with D156 and a $E_{\text{lab}} = 8.37$ MeV ^{12}C beam. The α peaks coming from the $^{12}\text{C}+^{12}\text{C}$ reaction are labelled as α_0 and α_1

tra in the energy regions where statistics were critically low (p_2 – p_6). A first fit was performed using four skewed Gaussian functions (as discussed previously). The second fit was done over the same energy region but using only three skewed Gaussian for p_3 to p_6 . The difference in χ^2 between both fits was of nearly 3σ demonstrating that the lowest statistics peak (typically, p_2) is indeed real.

Alpha channel

At the beam energies used in this work, only α_0 and α_1 had enough energy to completely pass through the Havar entrance window of the IC (only part of the α_2 group could pass the window, and was therefore not analyzed in this work). Low energy α particles (typically $E_\alpha < 7.10$ MeV, depending on angle) were stopped in the gas of the ionisation chamber and did not produce any signal in the silicon detectors. Unlike for the proton channel, data analysis for the α channel was therefore performed on reconstructed total energy spectra, ($E_{\text{tot}} = \Delta E + E_{\text{rest}}$). A sample of a background-subtracted spectrum is shown in Fig. 6.

To extract the number of events under each α peak, we followed the same approach used for the proton groups. Here, we fit the background-subtracted spectra with the sum of two skewed Gaussian functions (for the α peaks) and a third function (for the low energy part of the spectra) as shown by the solid curve in Fig. 6. In some cases, pile up appeared close to the α_0 peak, thus another skewed Gaussian was used to fit and subtract the events under this peak from the region of interest. The uncertainty on the number of events in each α peak was calculated as for the proton channel. Systematic errors are the same as for the proton analysis.

3.2 Cross-section evaluation from differential thick-target yields

From the net number of events N measured in each proton and alpha-particle peak, thick-target yields Y^∞ were calculated, at each beam energy E_b , as follows [50]:

$$Y^\infty = \frac{N q e}{\eta Q}, \quad (2)$$

where q and e are the charge state of the beam and the elementary charge, respectively; Q is the total charge collected on target during beam irradiation; and η is the detection efficiency.

To obtain the differential cross sections $d\sigma/d\Omega$, we differentiated the thick target yields Y^∞ measured at two consecutive beam energies, as:

$$\frac{d\sigma}{d\Omega} = \frac{\epsilon [Y^\infty(E_b) - Y^\infty(E_b - \Delta)]}{\Delta}, \quad (3)$$

where ϵ is the stopping power and Δ is the beam energy step, in this work 40–100 keV in the laboratory system.

The differential cross section was then associated to an effective energy E_{eff} , defined as (see [51] for the full derivation):

$$E_{\text{eff}} = E_b - \frac{1}{2}\Delta + \frac{[1 + R_2^2 \Delta^2/12]^{1/2} - 1}{R_2}, \quad (4)$$

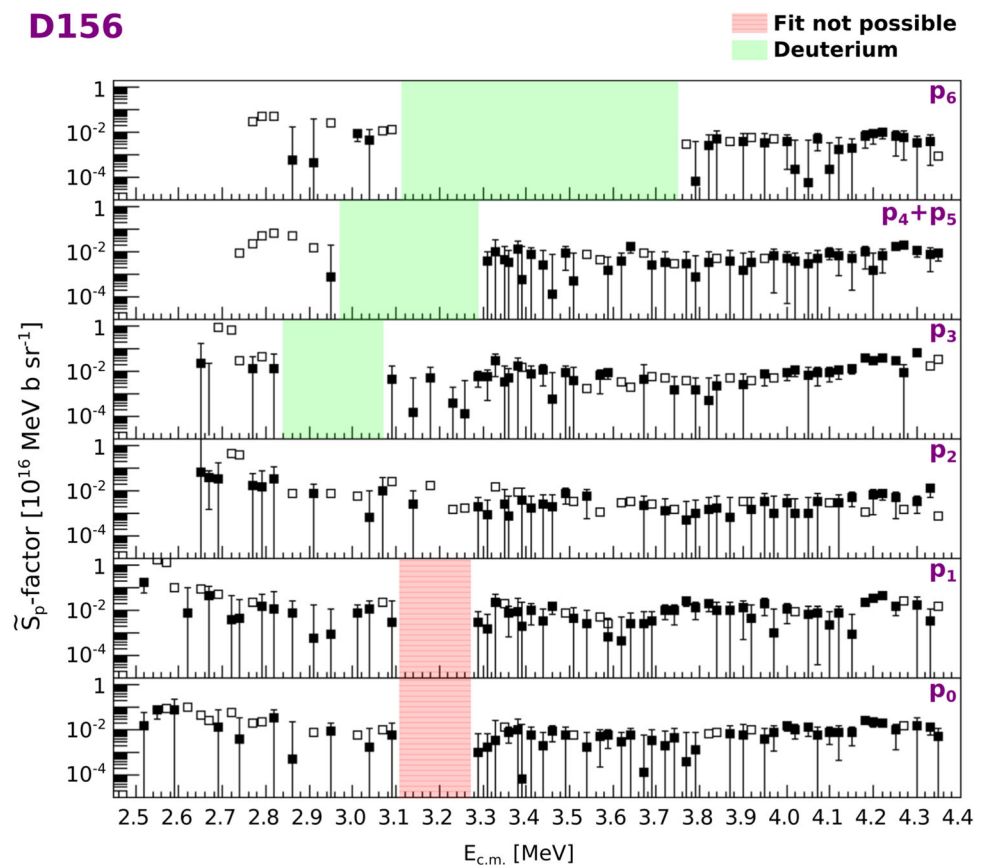
where $R_2 \equiv [(\frac{d^2\sigma_m}{d^2E})/(\frac{d\sigma_m}{dE})]_{E_h}$ is calculated for $E_h = E_b - \Delta/2$. Here, σ_m is a quadratic approximation of the cross section between the energies one step above and one step below the E_b being considered. The evaluation of R_2 would require the prior knowledge of σ_m and E_{eff} . It is practically computed by finite differences of σ_m values given by Eq. 3 and E_h at the current, previous and subsequent E_b .

Effective energies were finally expressed in the centre of mass system and the cross section (Eq. 3) converted into the modified \tilde{S} -factor [52]:

$$\tilde{S}(E) = E \sigma(E) \exp\left(\frac{87.236}{\sqrt{E}[\text{MeV}]} + 0.46 E[\text{MeV}]\right) \quad (5)$$

Typical uncertainties in E_{eff} were found to be ~ 12 keV (in the lab. system) by propagation of the beam energy uncertainty (~ 11 keV). Given that the energy step used in the present work is small, when using E_{eff} to evaluate R_2 rather than E_h the variation in the final results, and thus the corresponding uncertainty, is neglected being usually $< 0.1\%$

Fig. 7 Differential \tilde{S} -factors (in 10^{16} MeV b/sr) for individual proton groups as obtained with detector D156. Open symbols represent upper limits. Errors are statistical only



4 Results

Proton channel

Differential \tilde{S} -factors for individual proton groups were obtained for each detector as shown in Fig. 7 for D156 (figures for the other detectors and data are available in the Supplemental Material). Upper-limits are shown in the form of open symbols. Where data points are missing, this was due to either: (a) difficulties in the fitting procedure due to low statistics and/or poor kinematic discrimination between proton groups (red shaded stripped area); (b) overlap with the deuterium contaminant peak at different beam energies for different proton groups (green shaded area); or (c) low-energy protons (high proton-group number) being stopped in the entrance window of the detector.

As a result of these data gaps, one cannot arrive at the total astrophysical \tilde{S} -factor, i.e. summed over all proton groups, unless missing data can be recovered. In principle, this could be achieved by interpolating available data points under the assumption of constant \tilde{S} -factors over the relevant energy regions. To verify this assumption, we calculated a branching ratio for each proton group i defined as:

$$BR_i(E) = \frac{\tilde{S}_i(E)}{\tilde{S}_{\text{sum}}(E)} \tag{6}$$

at all those energies E where data from all proton groups are available, so that the sum \tilde{S}_{sum} of all partial \tilde{S} -factors could be calculated.

Branching ratios revealed significant variations as a function of energy as shown in Fig. 8 for data of p_0 from detector D156 (similar results were obtained for other proton groups and detectors). Given the impossibility to recover missing data, summed (over all proton groups) differential \tilde{S} -factors could only be obtained at energies where all the proton groups were observed (including cases where individual proton groups could not be separated).⁵

Summed differential \tilde{S} -factors for protons and α particles are shown in the supplemental material.

Alpha channel

Similar analysis procedures were adopted for the α channel. In this case, however, the $^{12}\text{C}+^1\text{H}$ reactions do not produce α particles within the region of interest, thus the extraction of cross sections for the $^{12}\text{C}(^{12}\text{C},\alpha)^{20}\text{Ne}$ reaction was more straightforward. Differential \tilde{S} -factors are shown for individual detectors and particle group in Fig. 9. Our results reveal

⁵ The only exception is at low centre of mass energies where proton groups from highly excited ^{23}Na nuclei are missing because of energy losses in the entrance windows.

Fig. 8 Branching ratios for p_0 group ($p_0/(p_0 + \dots + p_6)$) vs centre-of-mass energy as obtained with D156. Data points where one or more proton groups were missing are not shown. Branching ratios proved to be non-constant

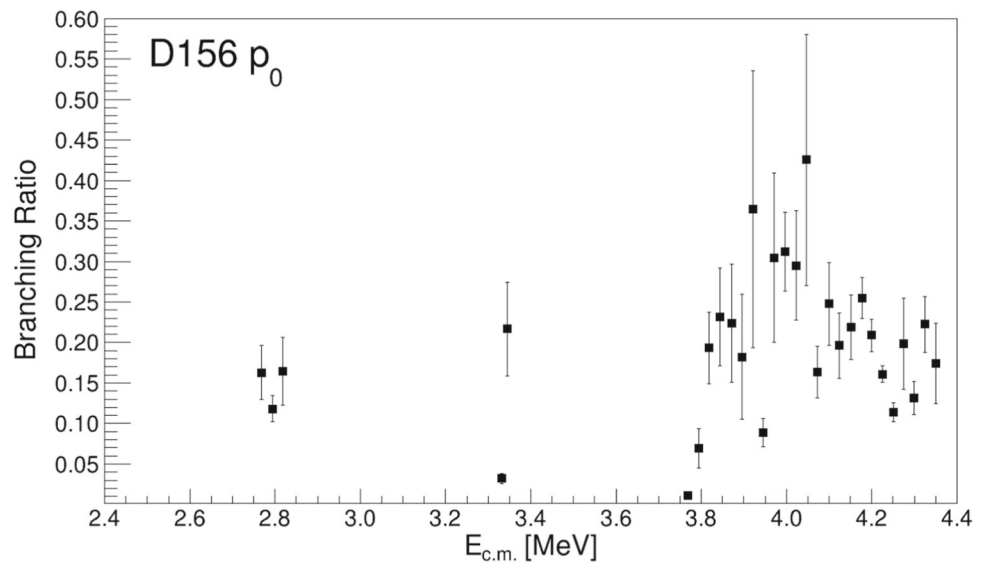
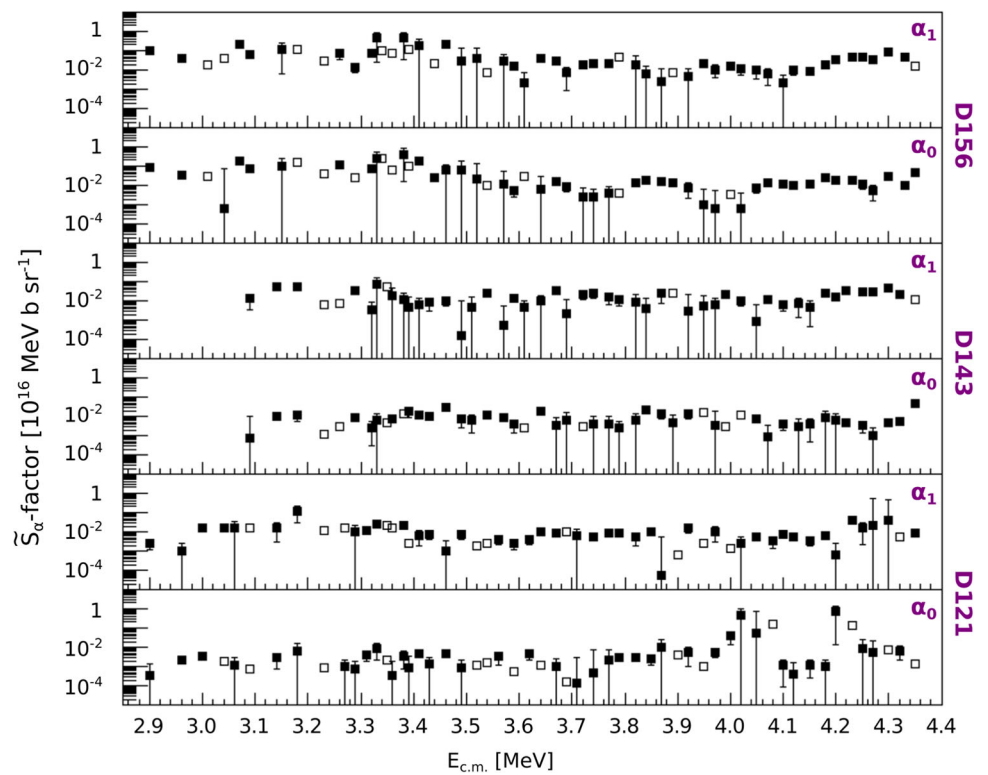


Fig. 9 Partial differential \tilde{S} -factors (in 10^{16} MeV b/sr), obtained with each GASTLY detectors for individual α_0 and α_1 groups, as a function of centre of mass energy. Errors are statistical only



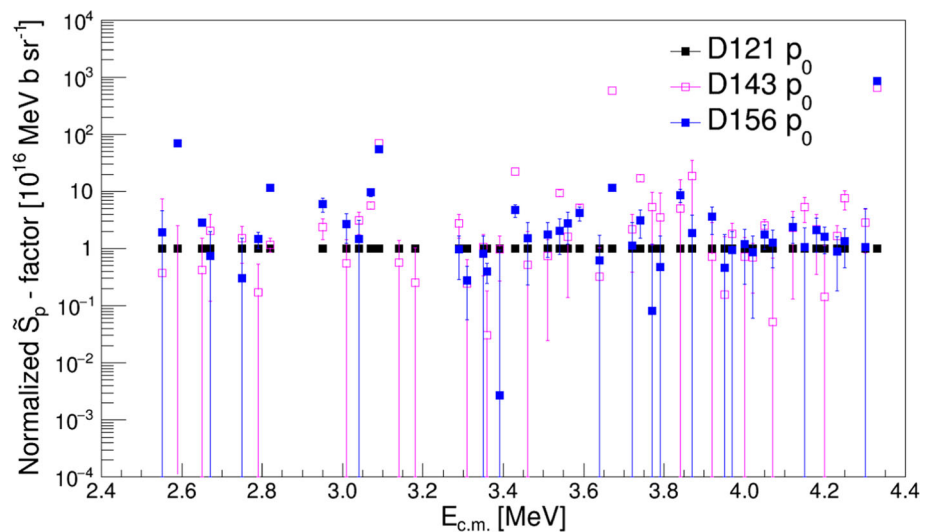
the presence of resonance-like structures across the entire energy region explored in this work, as also reported in previous studies [25,28,32,33,53].

5 Comparison with previous results and discussion

To compare our results with some of the total \tilde{S} -factors available in the literature, the angular distribution of individual proton- and α -particle groups should be studied. Unfortu-

nately, this was not possible with the limited angular range covered by our setup. Nevertheless, we tried to identify possible anisotropies by comparing angular distribution trends for each particle group as a function of energy. As an example, Fig. 10 shows the \tilde{S} -factors for p_0 at the three angles investigated as a function of centre of mass energy and normalised to the data taken with D121. Similar results were obtained for all proton- and α -particle groups. Despite the large error bars, these plots suggest the presence of anisotropies at all energies, such that total \tilde{S} -factors cannot be obtained by sim-

Fig. 10 Partial differential \tilde{S} -factors for p_0 as a function of centre of mass energy and for all three angles. Data are normalised to those obtained with D121 to emphasise possible anisotropies (see text for details)



ply integrating our summed differential \tilde{S} -factors over the full solid angle. These anisotropies might be the reason for inconsistencies among literature data sets.

This notwithstanding, we have attempted a *qualitative* comparison with selected⁶ data in the literature by *assuming* isotropic distributions for all protons and α -particle groups observed in this study. Results are displayed in Fig. 11 and show a general trend in qualitative agreement with that of other data sets. Should isotropy be confirmed, our data would only be consistent with those of Becker et al. [25] in the proton channel and lower than other selected data sets considered here in the α -channel at all energies.

Discrepancies between data sets are perhaps not entirely surprising given the challenging nature of these measurements and the difficulty of detecting rare events from heavy ion reactions at low energies. As anticipated, a possible cause for such disagreements may be found in strong anisotropies not properly taken into account and the limits of each experiment to detect one or more proton and α -particle groups. In addition, other effects may also play a role, such as for example, changes in the isotopic composition of the targets over time and/or the presence of beam-induced background difficult to account for. Despite considerable efforts to keep background contamination under control, clear deviations remain between our data set and those in the literature, whose origin is not fully understood. Future studies may therefore benefit from a careful investigation of target properties (e.g. through RBS, ERDA or NRA analyses) alongside the actual cross section measurements.

We conclude by noting that our data points have the smallest energy step to date. The results presented in this work supersede those in Ref. [45].

⁶ We have excluded data sets whose S -factors were not given in absolute units.

6 Summary and conclusions

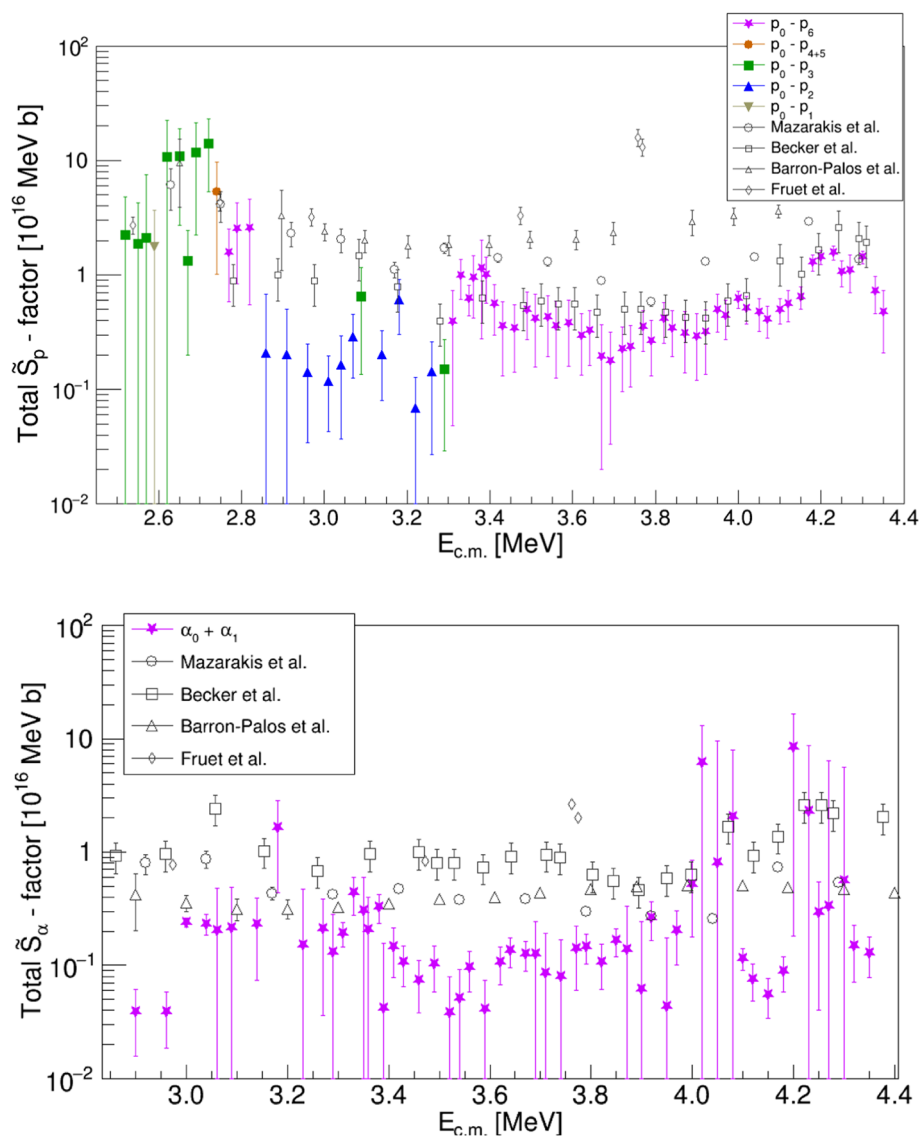
The $^{12}\text{C}+^{12}\text{C}$ fusion reactions are among the most important in astrophysics as they govern the evolution and fate of massive stars. Despite impressive experimental efforts over the last few decades we are still far from the required precision in their cross sections at stellar energies.

In this work, we reported on the measurement of the $^{12}\text{C}(^{12}\text{C},p)^{23}\text{Ne}$ and $^{12}\text{C}(^{12}\text{C},\alpha)^{23}\text{Na}$ reaction channels in the energy range $E_{\text{c.m.}} = 2.51\text{--}4.36$ MeV and with energy steps $\Delta E_{\text{c.m.}} < 25$ keV (the finest energy steps to date, to our knowledge). The experiment was performed at the CIRCE Tandem Accelerator Laboratory, using an array of four $\Delta E - E_{\text{rest}}$ detectors at backward angles for unambiguous particle identification. Thick highly ordered pyrolytic graphite targets were maintained at temperatures $\geq 400^\circ\text{C}$ to minimise deuterium contaminants and thus beam-induced background.

Background-subtracted proton- and α -particle spectra were fit with skewed Gaussian functions to obtain the net number of events under all particle peaks ($p_0 - p_6$ and $\alpha_0 - \alpha_1$). Cross sections were obtained by differentiating thick-target yields measured at consecutive beam energies and converted into differential \tilde{S} -factors for individual proton- and α -particle groups. These were finally summed over all particle groups.

Our results suggest the presence of resonance-like structures as also revealed by previous measurements. However, non-constant branching ratios and anisotropic angular distributions were observed for all particle groups at most energies, thus preventing the calculation of the total angular-integrated \tilde{S} -factors. As such, only qualitative comparisons with literature results were made for both proton- and α -groups. We note that existing discrepancies among various data sets available in the literature may indeed arise from incorrect

Fig. 11 Comparison of total proton (top) and alpha (bottom) \tilde{S} -factors obtained in this study (filled symbols) assuming isotropic angular distributions and selected data sets (open symbols): Mazarakis et al., Becker et al. [24,25] (angle integrated), Barron-Palos et al. and Fruet et al. [16,36] (assuming isotropic angular distributions)



assumptions on constant branching ratios and isotropic angular distributions.

Figures for individual proton groups and summed over all proton- and α -particle groups can be found in the Supplemental Material.

Improvements to our setup are currently underway to cover a wider angular range for angular distributions and to extend cross-section measurements to lower energies.

Acknowledgements This work was supported by the Italian National Institute of Nuclear Physics (INFN), V:ALERE, V:ANS and the Royal Society. MA acknowledges the support of a Visiting Professorship from the Università degli Studi della Campania “Luigi Vanvitelli”. LMG thanks CoNaCYT (scholarship 311745), the University of Edinburgh and COST Action ChETEC: CA16117 (STSM number 38819) for their financial support.

Funding Open access funding provided by Università degli Studi della Campania Luigi Vanvitelli within the CRUI-CARE Agreement.

Data availability This manuscript has data included as electronic supplementary material. The online version of this article contains supplementary material, which is available to authorized users.

Open Access This article is licensed under a Creative Commons Attribution 4.0 International License, which permits use, sharing, adaptation, distribution and reproduction in any medium or format, as long as you give appropriate credit to the original author(s) and the source, provide a link to the Creative Commons licence, and indicate if changes were made. The images or other third party material in this article are included in the article’s Creative Commons licence, unless indicated otherwise in a credit line to the material. If material is not included in the article’s Creative Commons licence and your intended use is not permitted by statutory regulation or exceeds the permitted use, you will need to obtain permission directly from the copyright holder. To view a copy of this licence, visit <http://creativecommons.org/licenses/by/4.0/>.

References

1. S. Cristallo et al., *J. Phys. (NPA6)* **665**, 012019 (2016)
2. M. Limongi, *Proceedings of Science (ENAS 6)*, p. 010 (2011)
3. E. Bravo et al., *Astron. Astrophys.* **535**, A114 (2011)
4. R.L. Cooper et al., *Astrophys. J.* **702**, 660 (2009)
5. M.E. Bennett et al., *Mon. Not. R. Astron. Soc.* **420**, 2737–2755 (2012)
6. B. Bucher et al., *EPJ Web Conf.* **93**, 03009 (2015)
7. A. Cumming, L. Bildsten, *Astrophys. J.* **559**, L127–L130 (2001)
8. X. Tang et al., *Nucl. Phys. At. Energy* **14**, 224–232 (2013)
9. Y. Sato et al., *Astrophys. J.* **807**, 105 (2015)
10. K. Mori et al., *Mon. Not. R. Astron. Soc. Lett.* **482**, L70–L74 (2019)
11. S.E. Woosley et al., *Astrophys. J.* **151**, 75–102 (2004)
12. I. Baraffè et al., *Astrophys. J.* **615**, 378–382 (2004)
13. F. Strieder, C. Rolfs, *Prog. Part. Nucl. Phys.* **59**, 562–578 (2007)
14. J.R. Patterson et al., *Astrophys. J.* **157**, 367–373 (1969)
15. M. Pignatari et al., *Astrophys. J.* **762**, 31 (2013)
16. L. Barrón-Palos et al., *Nucl. Phys. A* **779**, 318–332 (2006)
17. C. Angulo, *Lect. Notes Phys.* **764**, 253–282 (2009)
18. B.R. Fulton, *Contemp. Phys.* **40**, 299–311 (1999)
19. M. Freer, A.C. Merchant, *J. Phys. G Nucl. Part. Phys.* **23**, 261 (1997)
20. D.A. Bromley et al., *Phys. Rev. Lett.* **4**, 365 (1960)
21. L.J. Satkowiak et al., *Phys. Rev. C* **26**, 2027–2034 (1982)
22. C.L. Jiang et al., *Phys. Rev. Lett.* **110**, 072701 (2013)
23. M.E. Bennett et al., *Proceedings of Science (NIC XI)*, p. 182 (2010)
24. M.G. Mazarakis, Stephens, *Phys. Rev. C*, **7**, 1280–1287 (1973)
25. H.W. Becker et al., *Zeitschrift für Physik A At. Nucl.* **303**, 305–312 (1981)
26. J. Zickefoose et al., *Phys. Rev. C* **97**, 065806 (2018)
27. M.D. High, B. Čujec, *Nucl. Phys. A* **282**, 181 (1977)
28. K.U. Kettner et al., *Zeitschrift für Physik A At. Nucl.* **298**, 65–75 (1980)
29. P. Rosales, E.F. Aguilera, *Revista Mexicana de Física* **S4(49)**, 88–91 (2003)
30. L. Barrón-Palos et al., *Revista Mexicana de Física* **S2(50)**, 18–23 (2004)
31. L. Barrón-Palos et al., *Eur. Phys. J. A* **25**, 645–646 (2005)
32. E. Aguilera et al., *Phys. Rev. C* **73**, 064601 (2006)
33. T. Spillane et al., *Phys. Rev. Lett.* **98**, 122501 (2007)
34. C.L. Jiang et al., *Nucl. Instrum. Methods Phys. Res. Sect. A* **682**, 12–15 (2012)
35. C.L. Jiang et al., *Phys. Rev. C* **97**, 012801 (2018)
36. G. Fruet et al., *Phys. Rev. Lett.* **124**, 192701 (2020)
37. W.P. Tan et al., *Phys. Rev. Lett.* **124**, 192702 (2020)
38. A. Tumino et al., *Nature* **557**, 687–690 (2018)
39. A.M. Mukhamedzhanov et al., (2018). [arXiv:1806.05921v1](https://arxiv.org/abs/1806.05921v1)
40. A. Tumino et al., (2018). [arXiv:1807.06148](https://arxiv.org/abs/1807.06148)
41. F. Terrasi et al., *Nucl. Inst. Methods Phys. Res. B* **259**, 14–17 (2007)
42. L. Morales-Gallegos et al., *Eur. Phys. J. A* **54**, 132 (2018)
43. M. Romoli, L. Morales-Gallegos et al., *Eur. Phys. J. A* **54**, 142 (2018)
44. Canberra Industries Inc., Pips Silicon Detectors Catalogue. <http://www.canberra.com/products/detectors/pips-detectors-single-multiple.asp>
45. L. Morales-Gallegos, Carbon burning in stars: an experimental study of the $^{12}\text{C}(^{12}\text{C}, p)^{23}\text{Na}$ reaction towards astrophysical energies. University of Edinburgh Ph.D. Thesis (2017). <https://era.ed.ac.uk/handle/1842/28967>
46. L. Zhang, (2016) Private communication
47. C. Bruno et al., *Eur. Phys. J. A* **51**, 94 (2015)
48. J.F. Ziegler et al., *Nucl. Inst. Methods Phys. Res. B* **268**, 1818–1823 (2010)
49. National Electrostatics Corp., Instruction Manual No. ZHT068600 for AMS current integrator, Middleton (2004)
50. C. Iliadis, *Nuclear Physics of Stars* (Wiley-VCH, 2007)
51. C.R. Brune, D.B. Sayre, *Nucl. Inst. Methods Phys. Res. A* **698**, 49–59 (2013)
52. D.G. Yakovlev et al., *Phys. Rev. C* **82**, 044609 (2010)
53. J. Zickefoose, $^{12}\text{C} + ^{12}\text{C}$ Fusion: Measurement and Advances Toward the Gamow Energy, University of Connecticut Ph. D. Thesis (2010). <https://www.proquest.com/docview/908637546>